Gold doping of tin clusters: exo- vs. endohedral complexes

Gleditzsch, Martin; Pašteka, Lukáš F.; Götz, Daniel A.; Shayeghi, Armin; Johnston, Roy L.; Schäfer, Rolf

DOI:
10.1039/C9NR03233A

Document Version
Peer reviewed version

Citation for published version (Harvard):
Gleditzsch, M, Pašteka, LF, Götz, DA, Shayeghi, A, Johnston, RL & Schäfer, R 2019, 'Gold doping of tin clusters: exo- vs. endohedral complexes', *Nanoscale*, vol. 11, no. 27, pp. 12878-12888. https://doi.org/10.1039/C9NR03233A

Journal Name

ARTICLE TYPE

Cite this: DOI: 00.0000/xxxxxxxxxx

Gold Doping of Tin Clusters: Exo- or Endohedral Complexes†

Martin Gleditzsch,*[a] Lukáš F. Pašteka,[b], Daniel A. Götz[a], Armin Shayeghi[c], Roy L. Johnston[d] and Rolf Schäfer[a]

Received Date
Accepted Date

DOI: 00.0000/xxxxxxxxxx

We present molecular beam electric deflection experiments on neutral gold-doped tin clusters. The experimental Sn_NAu ($N = 6-16$) cluster beam profiles are interpreted by means of classical trajectory simulations supplied, with cluster structures generated by a genetic algorithm based on density functional theory. The combined experimental and theoretical analysis confirms that at least nine tin atoms are necessary to form a cage that is capable of encapsulating a gold atom, with high symmetry only marginally distorted by the gold atom. Two-component DFT calculations reveal that spin-orbit effects are necessary to properly describe these species. Partial charge analysis methods predict the presence of charge transfer effects from the tin host to the dopant, resulting in a negatively charged gold atom.

1 Introduction

The discovery of fullerenes[1] followed by their synthesis and macroscopic assembly, have confirmed that materials composed of clusters are very different from those composed of atoms or small molecules[2]. In C_{60} this results from an increased stability due to the spherical π-bonding of the carbon p electrons which makes them suitable for the assembly of even larger stable aggregates. This stability is attributed to spherical aromaticity[3], where electrons are delocalised over the entire cage structure. Fullerenes have been generated in pure and doped form by laser vaporization sources[1,4]. The heavier homologues of carbon are able to form cage structures as well; for example, lead based cage structures have been predicted[5] and reported in the gas phase[6] as well as in the solution[7]. The Sn_{12}^{2-} cluster[8] was found to be a remarkably stable cage with high I_h-symmetry, which allows its $5p$ electrons to delocalise over the complete cage and form π-bonds.[8] The bonding pattern was reported to be similar to the valence-isoelectronic $B_{12}H_{12}^{2-}$ molecule, which was the first synthesis[9] based on the stability prediction by molecular orbital theory[10]. The spherical aromaticity i.e., the spherical π-bonding, is the reason why the heavier group 14 clusters are discussed as the inorganic analogues of fullerenes[8,11,12]. The examination of isolated Sn_{12}^{2-} and Pb_{12}^{2-} in the gas phase was not possible up to now, even though a positive electron binding has been theoretically predicted[8]. Stabilization with an alkali metal atom is necessary and results in an endohedral incorporation of the dopant. The formation of $K@Sn_{12}^{-}$ or $K@Pb_{12}^{-}$ was observed in mass spectra and further investigated by photoelectron spectroscopy[8]. Formally, the stability of Sn_{12}^{2-} or Pb_{12}^{2-} can be justified in terms of the ionic resonance structures $K^+@Sn_{12}^{2-}$ or $K^+@Pb_{12}^{2-}$, respectively. The Sn_{12}^{2-} cage was reported to have a diameter of 6.1 Å and is thus only slightly smaller than the C_{60} fullerene, which has a diameter of 7.1 Å[2]. This is theoretically large enough to accommodate not only main group elements but also transition metals of the d- or even f-block elements[13].

Doping with alkaline earth metals leads to neutral species, e.g of the type $Mg@Sn_{12}$ or $Mg@Pb_{12}$. Electric deflection experiments show these species to be endohedral complexes with vanishing electrical dipole moments[14]. Typical transition metals such as manganese or iron are encapsulated in the same type of cage structure[15,16]. Though, for $Fe@Sn_{12}$ density functional theory (DFT) calculations and magnetic deflection measurements indicate that the iron dopant is not located exactly in the centre of the cage. However, doping with group 15 elements give examples to an entirely different behaviour. Here, the dopants are not endohedrally encapsulated but form part of the cluster cage, formally contributing an additional electron, leading to the overall structure mimicking the geometries of tin clusters with an increased negative charge[17]. The same observation applies to doping with

[a] Technische Universität Darmstadt, Eduard-Zintl-Institut, Alarich-Weiss-Straße 8, 64287 Darmstadt, Germany
[b] Department of Physical and Theoretical Chemistry & Laboratory for Advanced Materials, Faculty of Natural Sciences, Comenius University, Mlynská dolina, Ilkovičova 6, 84215 Bratislava, Slovakia
[c] Vienna Center for Quantum Science and Technology (VCQ), Faculty of Physics, University of Vienna, Boltzmanngasse 5, A-1090 Vienna, Austria
[d] School of Chemistry, University of Birmingham, Edgbaston, Birmingham B15 2TT, United Kingdom

† Electronic Supplementary Information (ESI) available: [details of any supplementary information available should be included here]. See DOI: 00.0000/00000000.

bismuth[18].

In this study, we have analysed the effect of late transition metal doping on the structure of tin clusters in detail. Specifically, we have examined the coinage metal gold. Similarly to alkali metals, coinage metals tend to form mono-charged cations, this suggests that clusters of the type $Au@Sn_{12}$ might be also described by an ionic structure such as $Au^{+}@Sn_{12}^{-}$. However, one needs to take the high electronegativity of gold into account. Whether this prevents the encapsulation of gold and leads to the formation of an ionic resonance structure, is the subject of this study. In this context, it is interesting to note that the cluster $[Au@Pb_{12}]^{3-}$ has been recently synthesized[19]. The quantum chemical investigation indicates that the mesomeric structure could be described as $Au^{-}@Pb_{12}^{2-}$, again indicating the formation of a Pb_{12}^{2-} cage.

In this article, a detailed study of the size-dependent evolution of the dielectric properties of neutral tin clusters doped with a single gold atom is presented. Electric deflection molecular beam profiles of Sn_NAu clusters have been recorded at the nozzle temperature T=20 K for N=7-16 and at T=40 K for N=6-16. The experimental results are supported by the DFT calculations for geometries obtained by a global geometry optimization based on a pool genetic algorithm[20]. Classical beam profile simulations based on the obtained geometries and their calculated dipole moments allow structural assignment.

2 Experimental Details

2.1 General

Electric beam deflection measurements have been established[15,21] as a reliable tool to probe the dielectric properties of neutral clusters in molecular beams. The presence of an inhomogeneous, electric field results in a deflection of the cluster beam. This beam deflection is due to both the permanent and the induced electric dipole moments, with the latter depending on the polarizability of the cluster.

However, it is not possible to extract directly the dielectric properties of the clusters from the measured beam profiles with and without electric field. The dielectric response depends on the shape of the cluster, i. e. the three moments of inertia, and on the magnitude of the interaction energy with the electric field strength with respect to the average rotational energy of the clusters. It is only possible to extract the approximate dielectric properties of the clusters with a perturbational theory approach. For a spherical, rigid rotor first order perturbation theory (FOPT)[22] can be applied, if the perturbation caused by the electric field is sufficiently small. In that case, the broadening of the cluster beam induced by the electric field allows one to determine the permanent electric dipole moment μ and the average beam deflection gives the value of the electronic polarizability α[21]. If FOPT is no longer justified, the obtained values for μ are still confidable, but the extracted values of α are wrong because the permanent dipole moment contributes significantly to the observed average beam deflection[23]. Therefore, reliable values for α could be only obtained if the clusters possess no permanent dipole moment. If the clusters are not spherical in shape, which is in almost all cases true, an analytical analysis of the measured beam profiles is not possible anymore[24]. Therefore, an approach based on the simulation of the rotational dynamics in the electric field has been developed. For that purpose the moments of inertia of the investigated cluster as well as the rotational temperature T_{rot} of a canonical cluster ensemble are needed as input parameters. The exact value of the rotational temperature is not known. It is, however, possible to narrow down the extent of the rotational temperatures influence by systematically studying the impact of T_{rot} on the beam profiles. Therefore the simulations allow one to predict the influence of the electric field taking quantum-chemically calculated moments of inertia into account. In this way the shape of the cluster and also the dielectric properties could be determined[22].

But, this approach still requires that the clusters could be treated as rigid rotors. If this is not the case, i. e. the clusters are vibrationally excited, the influence of the permanent electric dipole moment on the measured beam profiles is reduced and the beam broadening is partially quenched[21]. Thus, the vibrational temperature needs to be sufficiently cooled down. This effect is analysed in this work by measuring beam deflections for two different nozzle temperatures. If the measured beam profiles are only slightly influenced by the variation of the nozzle temperature this indicates that the clusters are nearly rigid and the measured beam profiles could be well compared with the trajectory simulations. Additionally, it has been shown that the velocity v_x of the clusters in the direction of the molecular beam is an indicator of T_{vib}[26]. Therefore, it is possible to estimate the vibrational temperature and to compare this value with typical frequencies of the vibrational normal modes calculated by quantum chemistry in order to decide if vibrational excitation is relevant for the performed experiments.

2.2 Details

The experimental setup has been described in detail elsewhere[15], only a brief overview is given here. Gold-doped tin clusters are generated by pulsed laser vaporization of an alloy target (15 atom-% Au in Sn). Helium is used as the carrier gas which enables cluster formation in an aggregation chamber. The cluster-helium mixture is cooled via a cryogenic nozzle (nozzle temperature T_{nozzle} = 20 K and 40 K) and expanded into high-vacuum. The supersonic expansion cools the various degrees of freedom of the clusters inside the molecular beam to a different extent. Under current experimental conditions, the rotational temperature T_{rot} is approximately 10 K[15]. However, vibrational degrees of freedom are less efficiently cooled[27].

It has been previously reported[15] that in our current experimental setup the assumption that the vibrational temperature T_{vib} is equal to T_{nozzle} is reasonable down to T_{nozzle} = 30 K. However, for lower values of T_{nozzle} thermalisation is not complete, probably due to short dwell times. The velocity v_x is measured with a mechanical chopper based on a solid state disk[28,29]. After expansion, the molecular beam passes two conical skimmers and is shaped into a rectangular profile by two collimating slits and afterwards enters an electric deflection unit (deflection voltage

$U = 20$ kV). After deflection, the clusters arrive at a scanning slit aperture, are photoionised by an F_2 excimer laser (7.9 eV) and are subsequently detected in a time-of-flight mass spectrometer.

3 Computational Details

To support the experimental data, a thorough global minimum search for each cluster size has been performed using the pool-Genetic-Algorithm (pool-GA)[20], based on the Birmingham Cluster Genetic Algorithm (BCGA)[30]. The genetic algorithm (GA) is coupled with the plane-wave self-consistent field density functional theory (PWscf DFT) module of the Quantum Espresso package[31]. Ultrasoft Rabe-Rappe-Kaxiras-Joannopoulos pseudopotentials[32] are employed to describe 54 core electrons for gold and 36 for tin. The remaining electrons are described explicitly with a cutoff energy of 40 Ry. Nonlinear corrections are applied and the Perdew-Burke-Ernzerhof (PBE) exchange-correlation (xc) functional[33] is used within the framework of spin restricted DFT. Additionally, a Methfessel-Paxton smearing[34] is used to improve the efficiency of electronic convergence. The geometry optimizations during the GA calculations are performed with an electronic self-consistency criterion of 10^{-6}eV, and total energy and force convergence threshold values of 10^{-4} eV and 10^{-3} eVÅ^{-1}, respectively. Convergence of the pool is achieved, when the minimum energy of the structures changes by less then 10^{-6}eV within 1000 structures. The generated structural candidates are then sorted by energy, interatomic distances and moments of inertia. All structural candidates within 0.5 eV of the energetic pool minimum are then subjected to further local optimization employing spin unrestricted orbital based DFT. These calculations are carried out at the scalar relativistic level with PBE0[35]/cc-PVTZ-PP[36,37], and its corresponding effective small core pseudo-potential with the NWChem package[38]. This basis set has been benchmarked against pure neutral and charged as well as against phosphorus-doped tin clusters[17] and all-electron scalar relativistic benchmark calculations[36,37]. The PBE0 functional is reported to 'perform exceedingly well'[39] and to give good agreement with experimental beam deflection data and coupled cluster calculations for pure neutral tin clusters[21,40]. These results were compared with calculations employing the def2-TZVPP[41,42] basis set and the TPSS[43] and B3P86[44,45] functionals. The electric dipole moments are calculated and vibrational analysis is performed. As the calculated relative energies depend on the level of theory, all isomers within a range of 0.1 eV are considered as possible experimental candidates or ground states. The calculated values of the electric dipole moments μ have to be treated carefully, since coupled cluster singles, doubles and perturbative triples (CCSD(T)) calculations for different Si_8 and Si_{11} isomers indicate that the results obtained by DFT calculations using various xc functionals vary from 10-20% with respect to the CCSD(T) benchmark calculations[46].

Classical beam deflection simulations[24,47] are applied using the calculated values of the electric dipole moment μ_i and moments of inertia I_i $(i = x,y,z)$ for all structural candidates. The simulations describe the rotational dynamics of an ensemble of rigid rotors (of any type) in an electric field for a given value of T_{rot}. This yields the dipole moment distribution function, which is convoluted with the experimental deflected beam profile[46] to generate the simulated beam profile. The latter can be compared to the experimental beam profiles to discriminate between structural candidates. To investigate the possible spin-orbit (SO) effects, two-component DFT calculations are performed using the DIRAC17 program package[48] for different iterations of the all-electron Dyall basis set family (v2z/v3z/av3z)[49–51] and the PBE0 functional[35].

4 Results and Discussion

4.1 Electric Deflection Measurements

In the mass spectrometric analysis of the tin-gold system, clusters with $N = 6-16$ tin atoms and $0-1$ gold atoms can be observed. An exemplary mass spectrum is shown in the Supporting Information†. Smaller doped species with $N = 6-9$ appear with low intensities in the mass spectra. Starting with ten tin atoms, the doped clusters are more stable in the mass spectrum. Larger as well as double-doped species are also abundant, but cannot be measured due to the low intensity in the beam and the broad isotopic distribution of tin. However, electric deflection experiments of Sn_NAu were successfully carried out for $N = 7-16$ at T_{nozzle}=20 K and $N = 6-16$ at T_{nozzle}=40 K. The corresponding experimental Sn_NAu beam profiles have been shown in Figure 1. Here the discrete experimental values of the beam profiles are fitted with a Gaussian, to acquire a continuous beam profile. It is important to consider possible thermal (vibrational) excitation, which would result in a fully or partially quenched electric dipole moment[25]. Thus, the experimentally obtained values for μ based on the beam broadening should be considered as lower limits on the true values. As mentioned in Section 2, the vibrational temperature T_{vib} of the clusters can be estimated based on their velocities. This analysis indicates that T_{vib} is up to 10 K higher than the corresponding T_{nozzle}. Figure 1 supplies further information on the extent of vibrational excitation. Since the species with $N = 9-12$ and $N = 8,13,14,16$ are shown to display no or minor thermal excitation between 20 K and 40 K, they are quite likely only negligibly vibrationally excited at 20 K. Thus, they can be considered as rigid at 20 K and thermal excitation is not expected to hinder the structural assignment via the trajectory simulations in Section 4.3.

The electric dipole moments extracted by first order perturbation theory (FOPT) for T_{nozzle} = 40 K are listed in Table 1. The FOPT analysis is only valid for spherical or weak symmetrical rotors and if the perturbation caused by the deflection field ($\vec{E}$) is sufficiently small ($|\vec{\mu}\cdot\vec{E}| << k_b T_{\text{rot}}$). For highly symmetrical or asymmetrical rotors and for species with strong dipole moments, the extracted values are incorrect. The measured beam profiles and the FOPT extracted values of μ at 40 K, already allow a few basic conclusions to be drawn. As the clusters $Sn_{10}Au$ and $Sn_{12}Au$ do not show beam broadening, they do not possess electric dipole moments. This indicates symmetrical structures where the gold atom is encapsulated in a highly symmetrical cage. The species $N = 9-12$ show no thermal excitation, while $N = 8,13,14,16$ show only negligible thermal excitation. For $N = 7,15$, there is a distinct influence of the nozzle temperature, which indicates the electric dipole moment to be at least partially quenched at 40 K, i.e. the

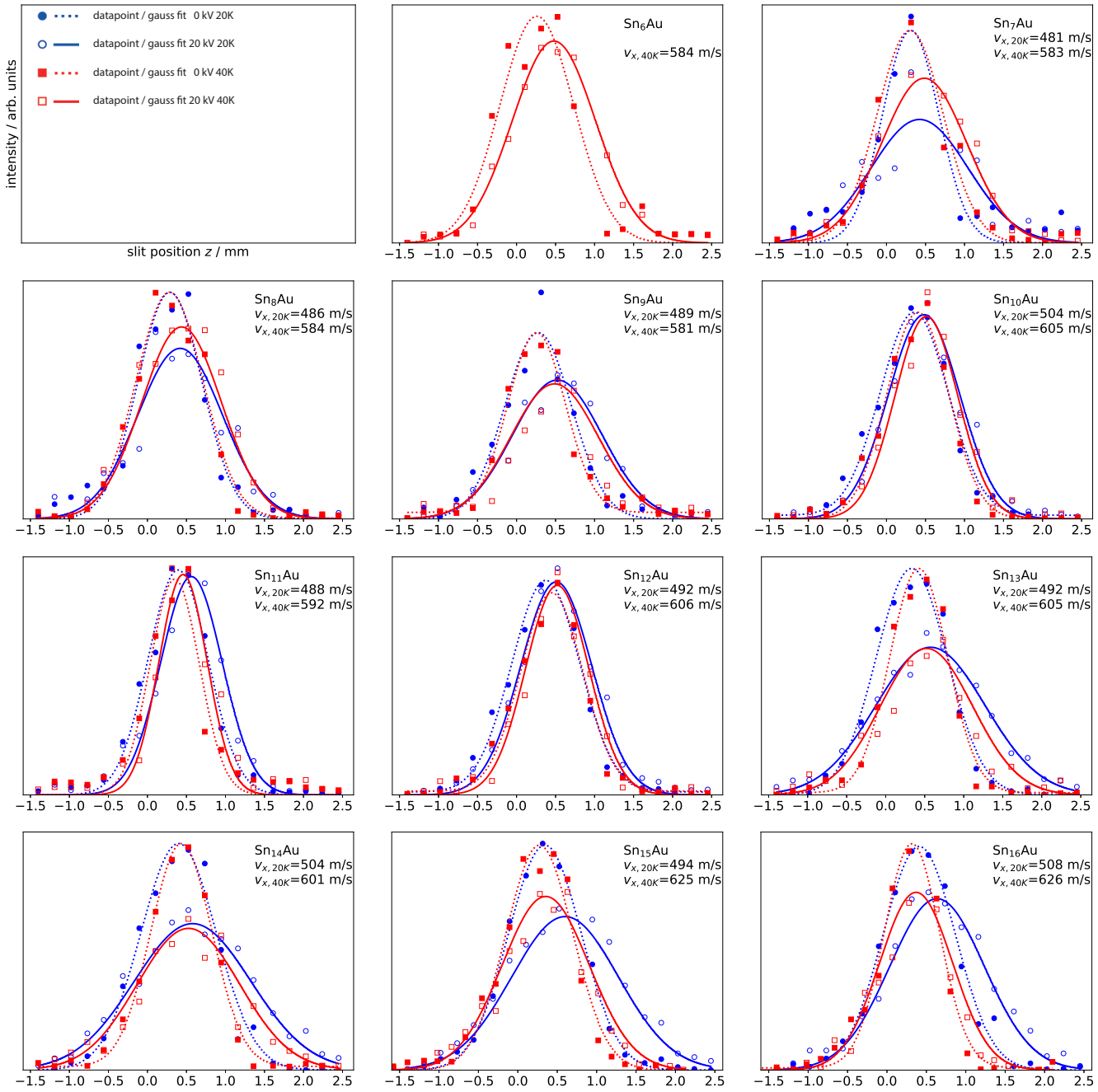

Fig. 1 Experimental electric deflection results for Sn_NAu, with T_{nozzle}=20 K (blue) and 40 K (red). The intensity profiles with electric field switched on (solid line) and off (dashed line) are fitted with Gaussians in order to extract the electric dipole moment by FOPT. The comparison of the beam profiles for different temperatures allows to draw conclusions on the extent of vibrational excitation which would result in a reduced broadening of the beam profile. While the species $N = 9-12$ and $N = 8, 13, 14, 16$ show no and minor thermal excitation, respectively, $N = 7, 15$ show a pronounced thermal effect. It is thus unlikely for most clusters to be vibrationally excited at 20 K and they can be considered as rigid when compared with the trajectory simulations.

obtained values for $\overline{\mu}$ based on FOPT for N= $N = 7, 15$ are larger at 20 K up to 30%. Starting with $N = 13$, significantly higher values of μ are observed, which suggests less symmetrical structural motifs for the clusters. In order to interpret these findings quantitatively, classical trajectory simulations need to be carried out.

Table 1 Results from the FOPT analysis of the experimental beam profiles at 40 K nozzle temperature. The average value ($\overline{\mu}$) of the electric dipole moment μ and its respective standard deviation σ_μ in Debye (D) have been taken over at least five different beam profiles, such as those shown in Fig. 1. Since the FOPT approximation assumes a spherical shape for the clusters, its application is questionable for symmetrical or asymmetrical rotors.

Cluster	$\overline{\mu}$	σ_μ
Sn_6Au	0.12	0.11
Sn_7Au	0.27	0.15
Sn_8Au	0.20	0.14
Sn_9Au	0.20	0.18
$Sn_{10}Au$	0.12	0.14
$Sn_{11}Au$	0.23	0.21
$Sn_{12}Au$	0.18	0.21
$Sn_{13}Au$	0.43	0.21
$Sn_{14}Au$	0.52	0.30
$Sn_{15}Au$	0.43	0.31
$Sn_{16}Au$	0.39	0.22

4.2 Structural Data I - Scalar Relativistic Calculations

Figure 2 depicts all calculated structural isomers with energies up to 0.1 eV above the predicted ground states (GS) for Sn_NAu clusters with $N = 6-16$. Structures up to 0.5 eV above the GS and a collection of all calculated cluster properties, are shown in the Supporting Information†. All structures display doublet multiplicities, as quartet isomers are at least 0.7 eV higher in energy. The vibrational modes of the predicted GS are depicted in Figure 3. Most species display their softest vibrational mode above 40 cm^{-1} and thus should not be thermally excited under the experimental conditions with T_{nozzle}=20 K. However, at 40 K, thermal excitation of soft vibrational modes is possible. The cluster Sn_6Au ($\widetilde{\nu}_{min}$=21 cm^{-1}) is an exception. The smaller clusters with $N = 6-8$ are shown to embed the gold dopant in their cage structure and seem to resemble the structures of $Sn_{N+1}^{0/+}$ to some extent[21,52]. This results in asymmetrical rotors for $N = 6-8$, which would make the application of FOPT to extract values of μ for these species problematic. Starting with $N = 9$, the gold dopant is endohedrally encased in the tin cage. Most of the endohedral GS structures are nearly-symmetrical rotors with two principle moments of inertia being almost equal. The species with $N = 12$ (spherical) and $N = 11, 14, 16$ (asymmetrical) are exceptions. The GS tin cage motifs of $N = 9-12$ resemble the anionic GS for Sn_9^-, Sn_{10}^-, Sn_{11}^-, Sn_{12}^- [53] and for $N = 9-13$ manganese-doped tin clusters[15]. The dipole moments of the gold-doped species with $N = 9, 11, 13$, however, are smaller than their manganese-doped counterparts. Since the species $Sn_{12}Au$ has the same structure as the hypothetical $Sn_{12}^-Au^+$, which would support the previously mentioned assumption where the gold dopant behaves similarly to an electro-positive alkali metal surrounded by a negative tin cage. However, in contrast to manganese, the heavier gold atom reduces the symmetry of the overall GS structure, resulting in a C_s point group for $N = 9, 11, 13-16$.

The ground state (GS) of Sn_6Au is a tricapped tetrahedron, with Au as one of the capping atoms. The energetically close isomer II is a tin-capped octahedron, with gold forming part of the octahedron. For Sn_7Au the GS is a pentagonal bipyramid with capping gold atom. This corresponds to a gold-capped $Sn_7^{0/+}$ GS or the $Sn_8^{0/+}$ GS with gold taking the place of the capping tin atom. The isomers of Sn_8Au are all based on pentagonal bipyramids and mimic the different $Sn_9^{0/+}$ isomers. In case of the GS and isomer II the gold dopant lies in the equatorial plane, resulting in the Sn_9^+ GS and isomer II, respectively. Isomer III is a permutational isomer (homotop) of the GS. Starting with $N = 9$, the gold dopants are endohedrally inserted resulting in tin cages which do not imitate the neutral or cationic pure tin analogues. For Sn_9Au, the tin cage closely mimics the Sn_9^- and Sn_9Mn GS. The $Sn_{10}Au$ GS also closely resembles the Sn_{10}^- and $Sn_{10}Mn$ GS, which results in a highly symmetric D_{4d} structure and a vanishing dipole moment. The same structural trend can be seen for the $Sn_{11}Au$ and $Sn_{12}Au$ GS, which also resemble the anionic pure tin and manganese-doped tin clusters.

Starting with $N = 13$, the structural motif differs from the Sn_N^- species. While $Sn_{13}Au$, which is a tin-capped icosahedron, still resembles the manganese-doped structures, the GS of $Sn_{14}Au$ represents a new structure. Here, the tin cage is more distorted and the additional tin atom is moved to the top, which results in a more asymmetrical rotor. The additional tin atom of the $Sn_{15}Au$ GS is added to the top and results in a near-symmetrical rotor. The structural motif of the $Sn_{16}Au$ GS is very similar to this, however again the additional tin atom at the top results in a more pronounced asymmetry of the principle moments of inertia. The low lying isomer II is also an asymmetrical rotor.

4.3 Structural Assignment with Trajectory Simulation

Trajectory simulations have been carried out for each isomer with rotational temperatures in the range $T_{rot} = 5-25$ K. As shown in the Supporting Information†, the influence of the value of T_{rot} is only minor. Thus, a value of $T_{rot} = 10$ K is applied which conforms to the previous work[16] and justifies the classical description of the rotational dynamics. As mentioned in Section 4.1, thermal excitation might quench the experimental beam broadening. This is clearly visible for most of the beam profiles at $T_{nozzle} = 40$ K (which exhibit $T_{vib} \approx 40-50$ K) and is supported by the results of the frequency analysis in Fig. 3. However, with the exception of Sn_6Au, the trajectory simulations were compared with the 20 K measurements and, therefore, for those species, no or negligible thermal excitations are expected. The differences between experimentally deflected and simulated beam profiles are quantified with the sum of squares due to error (SSE) method. Figure 4 shows the simulated beam profiles and comparison with the experimental beam profiles at $T_{nozzle} = 20$ K.

The simulated beam profiles for both Sn_6Au isomers match the

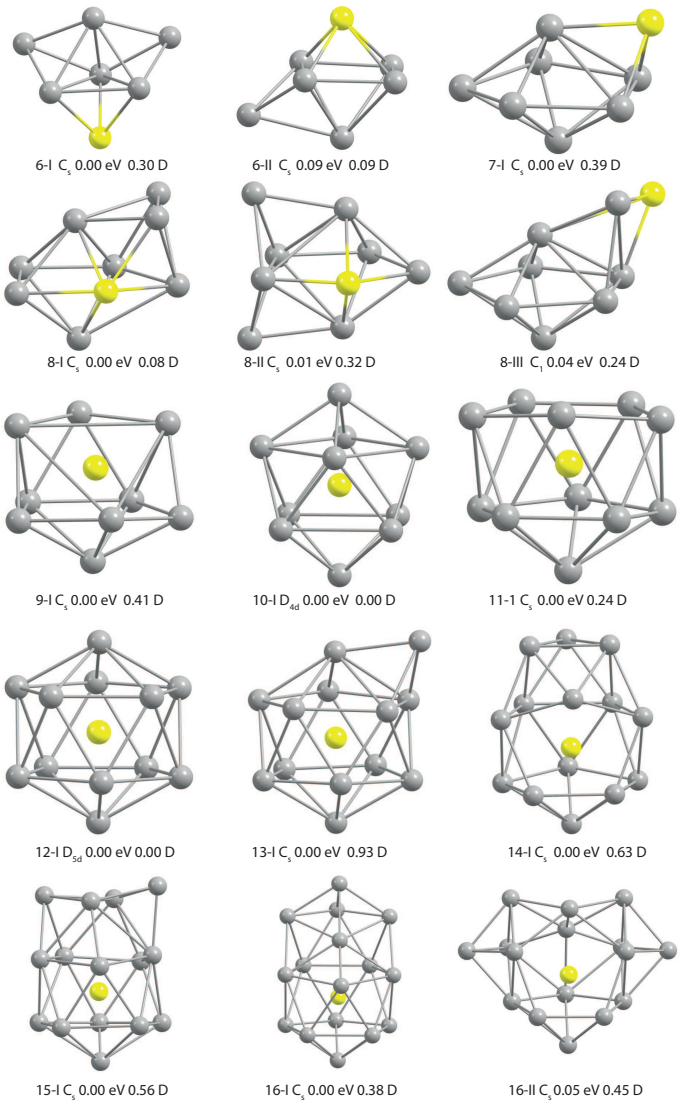

Fig. 2 Energetically low-lying isomers, up to 0.1 eV above the GS, for Sn_NAu with $N = 6-16$ as obtained at the PBE0/cc-PVTZ-PP scalar relativistic level of theory. The first number displays the number (N) of tin atoms, while the roman numeral denotes the isomer and is followed by its symmetry in Schönfließ notation, its relative energy in electronvolt (eV) and its absolute dipole moment in debye (D). Smaller clusters with $N < 9$ form exohedral structures and mimic to some extent pure tin clusters, with gold acting as a tin atom. Starting with $N = 9$ tin cages develop endohedral complexes with the gold dopant and mimic their manganese-doped counterparts from $N = 9-13$. Starting with $N = 14$, the tin cages take different shapes around the gold dopant.

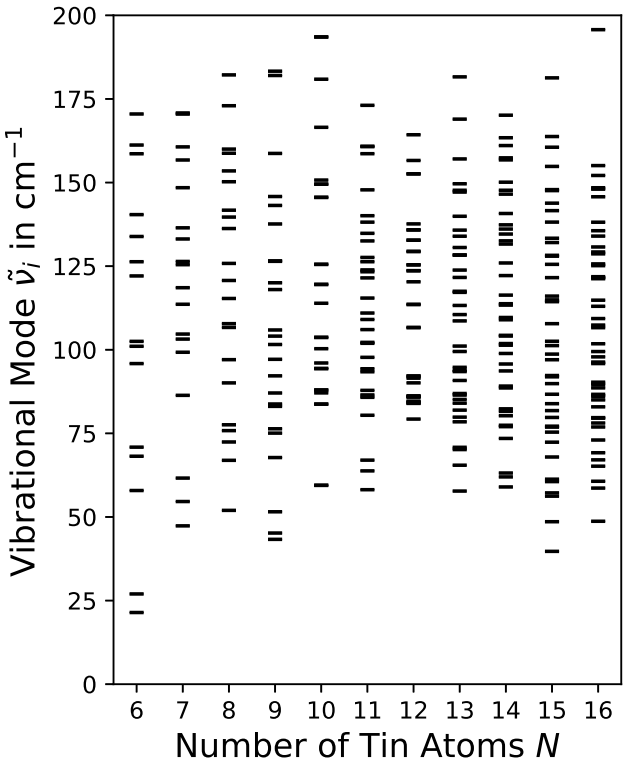

Fig. 3 Vibrational modes $\tilde{\nu}_i$ for Sn_NAu with $N = 6-16$ at the PBE0/cc-PVTZ-PP scalar relativistic level of theory. Most species display their softest vibrational mode above 40 cm^{-1} and thus should not be strongly thermally excited under experimental conditions at T_{nozzle}=20 K. The species Sn_6Au, however, is an exception and might display thermal excitation under experimental conditions, resulting in a reduced beam broadening.

experimental profiles reasonably well with SSE value of 0.023 for both. Because the experimental profile was recorded at 40 K and the cluster shows soft modes, a possible thermal effect has to be considered. However, both isomers only have relatively low dipole moments. Therefore, the thermal effect is quite small and a good agreement is obtained between experiment and theory. It is, thus, not possible to favour one candidate. For Sn_7Au, the sole predicted candidate describes the experimental beam profile well and is, therefore, a good candidate for the experimentally generated cluster. The simulated profile is not a proper Gaussian, which further indicates that FOPT is not entirely appropriate for this cluster under the experimental conditions of $T_{nozzle} = 20$ K. In the case of Sn_8Au, the GS profile with a SSE value of 0.150 can be excluded, while isomers II (0.081) and III (0.107) both describe the experiment equally well and are possible candidates. However, the lower energy of isomer II (only 0.01 eV above the putative GS) means this may be a better candidate. For Sn_9Au, the GS describes the experimental beam profile well and is a good candidate for the experimental structure. The deviation between experimental and simulated beam profile might be caused by the slight thermal excitation or the semi-empirical nature of the DFT functional. While both beam profiles for $Sn_{10}Au$ and $Sn_{12}Au$ show a vanishing dipole moment and perfectly matched by their theoretical GS, the beam profile for $Sn_{11}Au$ and $Sn_{13}Au$ are not properly described by the trajectory simulations. In both cases, the DFT dipole moments of the only possible candidates are considerably higher than the experimental dipole moments. Because the differences in measured beam profiles between $T_{nozzle} = 20$ K and 40 K are not pronounced enough, thermal effects are unlikely to be responsible for this. As shown in the Supporting Information†, the only identified isomer of $Sn_{13}Au$ with a low dipole moment is located over 0.4 eV above th GS. However, since gold is known for its relativistic properties, SO effects will be analysed and discussed in Section 4.4, particularly for $Sn_{11}Au$ and $Sn_{13}Au$. For $Sn_{14}Au$, the simulation again

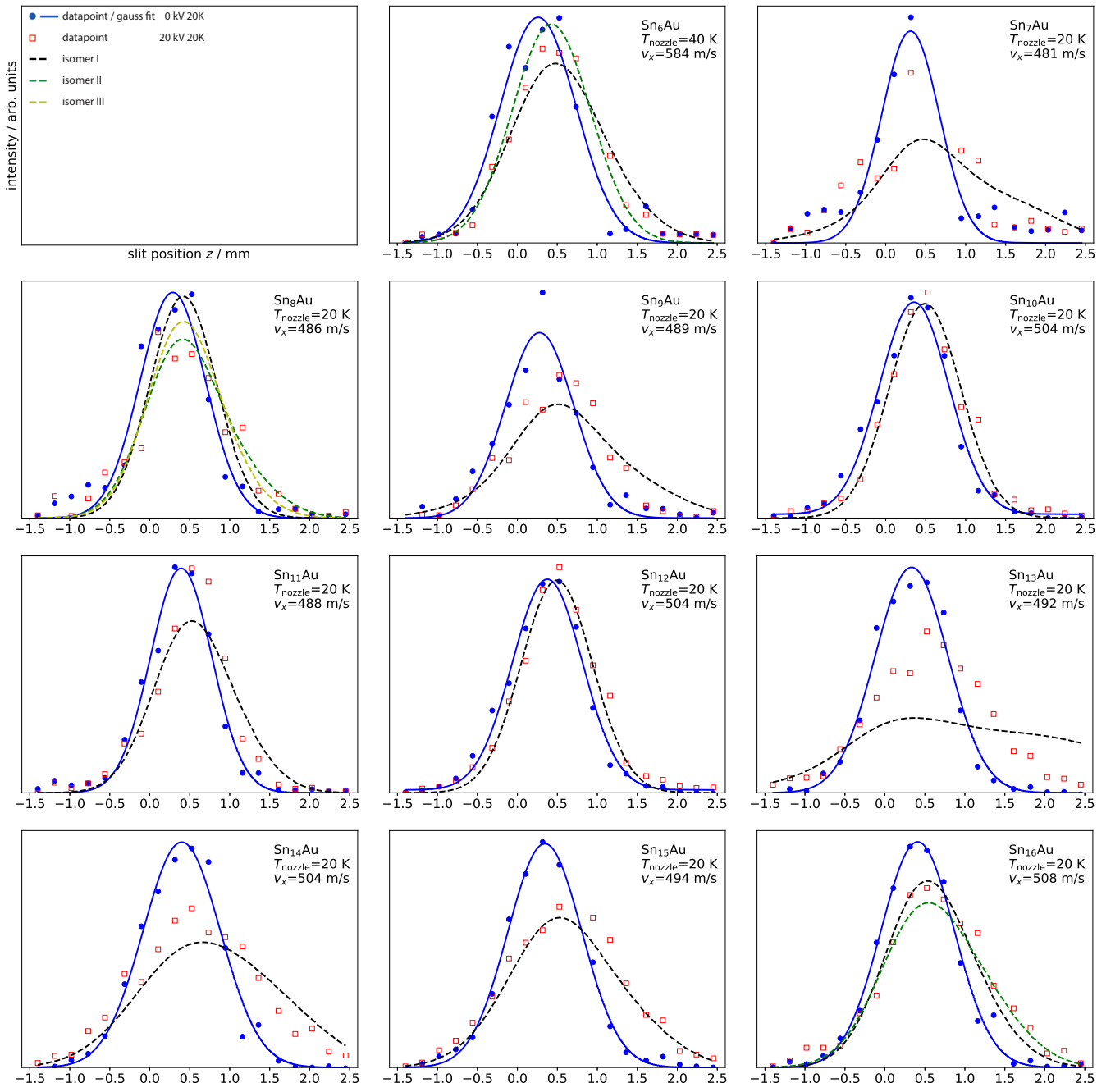

Fig. 4 Experimental electric deflection results, with $T_{\text{nozzle}} = 20$ K and, with the simulated beam profiles for the different isomers gold-doped tin clusters at the scalar-relativistic level of theory. The experimental data points with field switched off (blue) are fitted with a Gaussian (solid blue line). The experimental data points with field switched on (red) are compared with the different simulated beam profiles (dashed lines with the colours black, green and yellow). The results are quantified with the sum of squares due to error (SSE) method. The SSE values are mentioned in the corresponding text. Clear matches are visible for $N = 7, 9, 10, 12, 14, 15$ and there are multiple possible candidates for $N = 6, 8, 16$. In the case of $N = 11, 13$, it is not possible unambiguously to assign the experimental structure at the scalar-relativistic level of theory.

describes the experimental beam profile quite well. Again, the slight difference might either be low thermal excitation or the semi-empirical nature of the DFT functional. While for $Sn_{15}Au$ the GS gives a near perfect match to the experimental profile and is, therefore, a good candidate for the experimental structure, in the case of $Sn_{16}Au$ it is not possible to distinguish between the GS (0.089) and isomer II (0.052). Both isomers describe the experimental profile well and are thus both possible candidates.

To summarize these results: starting from $N = 9$ the gold atom is endohedrally encased in the tin cage and forms analogous structures to electropositive dopants.

4.4 Structural Data II - Spin Orbit and Basis Set Effects

The results of the two-component DFT calculations as well as the scalar relativistic cc-PVTZ-PP and Dyall-v3z calculations are summarized in Table 2. At the two-component level, the clusters retain the same structural motifs as in the scalar relativistic calculations, with only small differences in bond lengths observed. Consequently, the two-component calculations reveal only minor differences in relative energies and dipole moments (0-18 %). While these changes are of the same magnitude as the DFT functionals error, the effect of changing the basis set from cc-PVTZ-PP to Dyall-v3z (0-68 %) is more pronounced. Since the latter is a decontracted all-electron basis set, it is considered more flexible for an accurate description of the system. However, the error of the pseudo-potential approximation as in cc-PVTZ-PP is expected to be smaller than the overall error of the correlation part due to the used DFT functionals[54].

For Sn_6Au isomer II, the dipole moment grows with basis set change to Dyall-v3z and also increases slightly at the two-component level of theory. This makes isomer II a closer match to the experimental beam profile. However, as in Section 4.3, both candidates are too similar to be distinguished based on the measured beam profiles. In Sn_7Au, the basis set change enlarges the dipole moment which is nearly fully compensated by the SO effect. For Sn_8Au, the energetic order of the nearly degenerated isomers I and II is already switched for Dyall-v3z at the scalar relativistic level. While the SO effect on the values of the dipole moments is nearly zero, isomer III is energetically slightly shifted out of the 0.1 eV range and is thus not considered anymore as a potential experimental species. This leaves isomer I as the only possible experimental structure for Sn_8Au. In the case of Sn_9Au, the basis set effect is again far more pronounced (16 %) compared to the SO effect (2 %), which results in an increased dipole moment. While this is not reflected in the experimental beam profile, low thermal excitation might partially quench the beam broadening. The $Sn_{11}Au$ cluster however displays a pronounced basis set and SO effect, both resulting in a significantly reduced dipole moment. The structure is more symmetrical at the two-component level of theory, which results in a reduced dipole moment. This is clearly reflected in the experimental beam profiles. The mismatch between the experiment and the scalar relativistic level of theory is thus not caused by thermal excitation, as already suggested in Section 4.3. The importance of SO effects for this species is quite interesting, but not clearly understood, since the other clusters do not show any such effect. Thus, much like Sn_9Au and $Sn_{13}Au$ the cluster display a lower dipole moment than its manganese-doped counterpart.

For $Sn_{13}Au$, neither the basis set nor the SO effects are pronounced. Since thermal excitation also cannot explain the mismatch between theory and experiment, a likely explanation is that the GA was unable to find the isomer observed in the experiment. Thus, the structural assignment of $Sn_{13}Au$ remains a challenge. For $Sn_{14}Au$ and $Sn_{15}Au$, basis set and SO effects are negligible so the structural assignment is already possible at the cc-PVTZ-PP-1c level of theory. For $Sn_{16}Au$, both isomers I and II display a slight basis set dependence, resulting in closer dipole moment values of both species with Dyall-v3z. Thus, even more so than on the scalar cc-PVTZ-PP-1c level, both isomers are experimentally indistinguishable. To summarize, it is thus possible to describe all gold-doped tin clusters with the exception of $Sn_{13}Au$ at the two-component level very well. A clear identification of the GS is in principle possible. However, in the cases of Sn_8Au and $Sn_{16}Au$, two isomers fit the experiment equally well.

Table 2 Comparison of the cc-pVTZ-PP-1c results with Dyall-v3z at the 1c and 2c level of theory. The first column shows the label of the cluster, followed by ΔE the energy relative to the minimum in electron volt (eV) and the electric dipole moment in Debye (D) for each level of theory, respectively. The table reveals for most species only minor SO effects and a pronounced basis set effect. Noticeable exceptions are isomer 8-III, with an SO induced effect on the relative energy and 11-I, with an SO induced lowering of the dipole moment. The latter is especially interesting, since it is necessary to explain the experimental results for $Sn_{11}Au$.

	cc-pVTZ-PP-1c		Dyall-v3z-1c		Dyall-v3z-2c	
Label	ΔE/eV	μ/D	ΔE/eV	μ/D	ΔE/eV	μ/D
6-I	0.00	0.30	0.00	0.30	0.00	0.29
6-II	0.09	0.09	0.07	0.15	0.07	0.18
7-I	0.00	0.39	0.00	0.48	0.00	0.40
8-I	0.00	0.08	0.01	0.09	0.01	0.10
8-II	0.01	0.32	0.00	0.33	0.00	0.33
8-III	0.04	0.24	0.08	0.27	0.10	0.26
9-I	0.00	0.41	0.00	0.47	0.00	0.46
10-I	0.00	0.00	0.00	0.00	0.00	0.00
11-I	0.00	0.24	0.00	0.18	0.00	0.15
12-I	0.00	0.00	0.00	0.00	0.00	0.00
13-I	0.00	0.93	0.00	0.91	0.00	0.88
14-I	0.00	0.63	0.00	0.65	0.00	0.64
15-I	0.00	0.56	0.00	0.58	0.00	0.57
16-I	0.00	0.38	0.00	0.39	0.00	0.41
16-II	0.05	0.45	0.01	0.41	0.06	0.41

5 Discussion and Conclusions

We have investigated the dielectric properties of isolated neutral gold-doped tin clusters Sn_NAu ($N = 6-16$) for different nozzle temperatures (20 K and 40 K). The electric beam deflection experiments reveal pronounced thermal excitations for $N = 7, 15$ between 20 K and 40 K, which is in good agreement with the frequency analysis of the predicted ground states. This emphasizes the need for cryogenic conditions, as already at 40 K, the thermal excitation hinders the structural assignment.

Two component DFT calculations reveal for most species only minor SO effects. However, for Sn_8Au, the energy shift allows the experimentally detected species to be distinguished. Interestingly, the $Sn_{11}Au$ cluster shows a more pronounced SO effect, which leads to a more symmetric structure with a reduced dipole moment. This is also reflected in the experimental beam profile and was previously attributed to possible thermal excitation. The structural assignment of $Sn_{13}Au$, however, remains a challenge, as neither the thermal excitation nor SO effects explain the deviation between theory and experiment. A likely explanation is that the GA was unable to find the experimental

isomer. Deflection experiments on copper-doped tin clusters are in preparation, as the less electronegative and lighter dopant might result in a different charge distribution in the clusters. Additionally, the comparison of $Sn_{11}Au$ and $Sn_{11}Cu$ would allow the dopant-induced and host-inherent SO effects to be distinguished.

The experimental investigations of Sn_NAu, together with the dielectric rotational dynamics simulation, show that with increasing cluster size the gold-dopant is endohedrally encapsulated for $N \geq 9$. It is interesting that the electric dipole moments do not reflect this structural change. Exceptions are the two highly symmetric clusters $Sn_{10}Au$ and $Sn_{12}Au$, with D_{4d} and D_{5d} symmetry, respectively, which for reasons of symmetry cannot possess an electric dipole moment. Otherwise, exo- and endohedral gold-doped tin clusters show similar values of the electric dipole moments. This does not initially correspond to expectation, since in a comparable binding situation the exohedral clusters should be significantly more polar. In order to better understand this situation, the charge distribution in the clusters was studied more accurately employing quantum chemical methods. This was done using the latest variant of the density derived electrostatic and chemical (DDEC6) approach, in order to calculate the net atomic charges (NAC) and bond orders[55]. It has already been shown in the literature that this procedure is well suited to describe endohedrally-doped fullerene clusters[56]. Figure 5 shows how these properties change with the number of tin atoms N. It is striking that in the exohedral cluster structures the Au atoms have only very low negative NAC values. Thus, the observed dipole moments of these species do not result from particularly polar Au-Sn bonds, but additionally from the uneven charge distribution across the tin atoms. In the endohedrally-doped clusters, the central gold atom is much more negatively charged. However, the observed dipole moments here depend on how much the symmetry of the tin cage deviates from an ideal-spherical charge distribution. As a result, as for $Sn_{10}Au$ and $Sn_{12}Au$, the dipole moments may disappear completely or have similar numerical values, as in the case of the exohedral cluster structures. The dipole moments not being deductible from the structural transition is due to the fact that the NACs of the Au are smaller in the exohedral structures than in the endohedral-doped clusters, and thus the effects of the structural transition on the dipole moment are masked. The altered bonding situation is also noticeable in the sum bond of the orders (SBO) of the gold atom. Starting with the exohedral clusters Sn_6Au or Sn_7Au SBO values close to two are found, in contrast the SBOs of Au for all endohedrally doped clusters from Sn_9Au to $Sn_{16}Au$ are close to four or even higher. The SBO of the tin atoms do not reflect any dependency on the cluster size, as its average values stay consistently between two and three. Additionally, the structural transition is also evident from the spin densities, since for exohedral clusters significantly increased values are predicted. In contrast, the endohedral compounds, with the exception of Sn_9Au, show virtually no spin density at the doping atom. Moreover, the values of the predicted spin densities are also very consistent if a different approach is chosen for the partial charge analysis techniques (see Supporting Information†) and

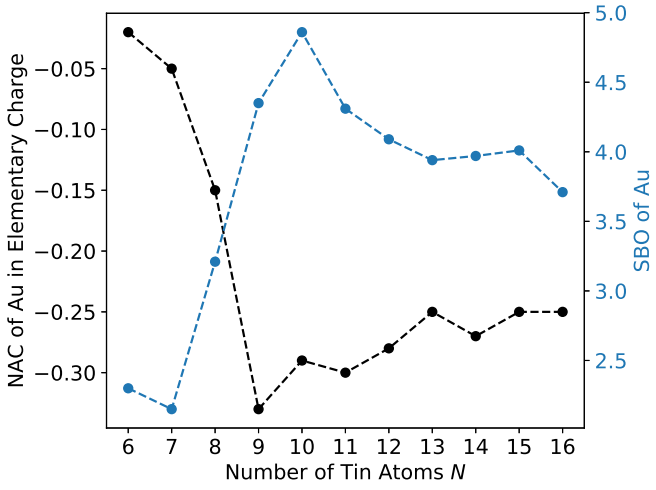

Fig. 5 Net Atomic Charges (NAC, black) and sum of the bond order (SOB, blue) for the gold dopants as obtained by the density derived electrostatic and chemical (DDEC6) approach as a function of the number of tin atoms N. The gold dopants display consistently negative NAC, however, they are relatively low for exohedral clusters in particular and thus, the electric dipole moments of the clusters are not caused by a particularly high polarity of the Au-Sn bonds, but additionally by an uneven charge distribution in the tin host. The SBO of the gold atom further reflects the structural transition with the gold atom being higher coordinated in the endohedral complexes. Thus, both properties reflect the change from exohedral to endohedral complexes.

are therefore particularly meaningful parameters for the observed change in the structural motif. This does not apply to the same extent for the calculation of NACs (see Supporting Information†). Although the NACs of Löwdin, natural bond order (NBO) and Bader charge analysis[57] show that the gold atoms are negatively charged, and they also show the same trend, namely that the value of the negative charge increases when the structural motif changes, but the absolute values are distinctly different. For the Bader and NBO approach in particular, significantly larger negative NACs are predicted for the dopant atom. To return to the initial question whether a cluster of the $Au@Sn_{12}$ type is formed and whether the charge distribution is similar to that of an electropositive doping atom, it can be concluded that the combination of electrical deflection measurements and global structure optimization can clearly prove that the gold atom in $Sn_{12}Au$ is endohedrally located. However, the value of the partial charge at the central gold atom cannot be unambiguously determined by the procedure employed. Quantum chemical studies on the bonding situation, however, indicate that the Au atom differs fundamentally from electropositive metals, and thus the initially postulated mesomeric resonance structure $Au^+@Sn_{12}^-$ does not correctly reflect the charge distribution.

Conflicts of interest

There are no conflicts to declare.

Acknowledgements

We acknowledge financial support by the DFG (SCHA 885/15-1). The calculations reported here were performed on the Lichten-

berg high performance computer of the TU Darmstadt, ARCHER, the UK National Supercomputing Service via membership of the UK's HPC Materials Chemistry Consortium, which is funded by EPSRC (EP/L000202), the Biby cluster resources[58] and the HPC cluster Peregrine of the Center for Information Technology, University of Groningen. LFP acknowledges the support from the Slovak Research and Development Agency (APVV-15-0105). We are thankful to G. G. Rondina for useful discussions and technical support.

Notes and references

1 H. W. Kroto, J. R. Heath, S. C. O'Brien, R. F. Curl and R. E. Smalley, *Nature*, 1985, **318**, 162–163.

2 P. Jena, *J. Phys. Chem. Lett.*, 2013, **4**, 1432–1442.

3 A. Hirsch, Z. Chen and H. Jiao, *Angew. Chemie - Int. Ed.*, 2001, **40**, 2834–2838.

4 J. R. Heath, S. C. O'Brien, Q. Z. Y. Liu, R. F. Curl, F. K. Tittel, R. E. Smalley and H. W. Kroto, *J. Am. Chem. Soc.*, 1985, **107**, 7779–7780.

5 L. F. Cui, X. Huang, L. M. Wang, J. Li and L. S. Wang, *J. Phys. Chem. A*, 2006, **110**, 10169–10172.

6 S. Neukermans, E. Janssens, Z. F. Chen, R. E. Silverans, P. V. R. Schleyer and P. Lievens, *Phys. Rev. Lett.*, 2004, **92**, 163401–1.

7 E. N. Esenturk, J. Fettinger, Y.-F. Lam and B. Eichhorn, *Angew. Chemie Int. Ed.*, 2004, **43**, 2132–2134.

8 L. F. Cui, X. Huang, L. M. Wang, D. Y. Zubarev, A. I. Boldyrev, J. Li and L. S. Wang, *J. Am. Chem. Soc.*, 2006, **128**, 8390–8391.

9 A. R. Pitochelli and F. M. Hawthorne, *J.Am.Chem.Soc.*, 1960, **82**, 3228–3229.

10 H. Longuet-Higgins and M. d. V. Roberts, *Proc. R. Soc. London*, 1955, **230**, 110–119.

11 X. Chen, K. Deng, Y. Liu, C. Tang, Y. Yuan, W. Tan and X. Wang, *J. Chem. Phys.*, 2008, **129**, 094301.

12 S. Furuse, K. Koyasu, J. Atobe and A. Nakajima, *J. Chem. Phys.*, 2008, **129**, 064311.

13 L. F. Cui, X. Huang, L. M. Wang, J. Li and L. S. Wang, *Angew. Chemie - Int. Ed.*, 2007, **46**, 742–745.

14 S. Schäfer and R. Schäfer, *ChemPhysChem*, 2008, **9**, 1925–1929.

15 U. Rohrmann, P. Schwerdtfeger and R. Schäfer, *Phys. Chem. Chem. Phys.*, 2014, **12**, 23952–23966.

16 U. Rohrmann and R. Schäfer, *J. Phys. Chem. C*, 2015, **119**, 10958–10961.

17 M. Gleditzsch, T. M. Fuchs and R. Schäfer, *J.Phys. Chem. A*, 2019, 1434–1444.

18 S. Heiles, R. L. Johnston and R. Schäfer, *J. Phys. Chem. A*, 2012, **116**, 7756–7764.

19 L. J. Li, F. X. Pan, F. Y. Li, Z. F. Chen and Z. M. Sun, *Inorg. Chem. Front.*, 2017, **4**, 1393–1396.

20 A. Shayeghi, D. Götz, J. B. A. Davis, R. Schäfer and R. L. Johnston, *Phys. Chem. Chem. Phys.*, 2015, **17**, 2104–2112.

21 B. Assadollahzadeh, M. Mehring, P. Schwerdtfeger and R. Schäfer, *J. Phys. Chem. A*, 2008, **112**, 12312–12319.

22 S. Heiles and R. Schäfer, *Dielectric Properties of Isolated Clusters*, Springer, 2014.

23 M. Schnell, C. Herwig and J. A. Becker, *Zeitschrift fr Phys. Chemie*, 2003, **217**, 1003–1030.

24 S. Heiles, S. Schäfer and R. Schäfer, *J. Chem. Phys.*, 2011, **135**, 034303.

25 S. M. Kast, S. Schäfer and R. Schäfer, *J. Chem. Phys.*, 2012, **136**, 134320.

26 U. Rohrmann and R. Schäfer, *Phys. Rev. Lett.*, 2013, **111**, 133401.

27 B. A. Collings, A. H. Amrein, D. M. Rayner and P. A. Hackett, *J. Chem. Phys.*, 1993, **99**, 4174.

28 L. P. Maguire, S. Szilagyi and R. E. Scholten, *Rev. Sci. Instrum.*, 2004, **75**, 3077.

29 S. Schäfer, *PhD thesis*, TU Darmstadt, 2008.

30 S. Heiles, A. J. Logsdail, R. Schäfer and R. L. Johnston, *Nanoscale*, 2012, **4**, 1109–1115.

31 P. Giannozzi, S. Baroni, N. Bonini, M. Calandra, R. Car, C. Cavazzoni, D. Ceresoli, G. L. Chiarotti, M. Cococcioni, I. Dabo, A. Dal Corso, S. de Gironcoli, S. Fabris, G. Fratesi, R. Gebauer, U. Gerstmann, C. Gougoussis, A. Kokalj, M. Lazzeri, L. Martin-Samos, N. Marzari, F. Mauri, R. Mazzarello, S. Paolini, A. Pasquarello, L. Paulatto, C. Sbraccia, S. Scandolo, G. Sclauzero, A. P. Seitsonen, A. Smogunov, P. Umari and R. M. Wentzcovitch, *J. Phys. Condens. Matter*, 2009, **21**, 395502.

32 A. M. Rappe, K. M. Rabe, E. Kaxiras and J. D. Joannopoulos, *Phys. Rev. B*, 1990, **41**, 1227–1230.

33 J. P. Perdew, K. Burke and M. Ernzerhof, *Phys. Rev. Lett.*, 1996, **77**, 3865–3868.

34 M. Methfessel and A. T. Paxton, *Phys. Rev. B*, 1989, **40**, 3616–3621.

35 J. P. Perdew, J. Tao, V. N. Staroverov and G. E. Scuseria, *J. Chem. Phys.*, 2004, **120**, 6898–6911.

36 K. A. Peterson, *J. Chem. Phys.*, 2003, **119**, 11099–11112.

37 K. A. Peterson and C. Puzzarini, *Theor. Chem. Acc.*, 2005, **114**, 283–296.

38 M. Valiev, E. J. Bylaska, N. Govind, K. Kowalski, T. P. Straatsma, H. J. J. Van Dam, D. Wang, J. Nieplocha, E. Apra, T. L. Windus and W. A. De Jong, *Comput. Phys. Commun.*, 2010, **181**, 1477–1489.

39 M. Bühl, C. Reimann, D. A. Pantazis, T. Bredow and F. Neese, 2008, 1–21.

40 P. S. BEHNAM ASSADOLLAHZADEH, SASCHA SCHÄFER, *J. Comput. Chem.*, 2009, **28**, 73–86.

41 F. Weigend and R. Ahlrichs, *Phys. Chem. Chem. Phys.*, 2005, **7**, 3297–305.

42 B. Metz, H. Stoll and M. Dolg, *J. Chem. Phys.*, 2000, **113**, 2563–2569.

43 J. Tao, J. P. Perdew, V. N. Staroverov and G. E. Scuseria, *Phys. Rev. Lett.*, 2003, **91**, 146401.

44 J. Perdew, *Phys. Rev. B*, 1986, **33**, 8822–8824.

45 A. D. Becke, *J. Chem. Phys.*, 1993, **98**, 5648–5652.

46 S. Heiles, *PhD thesis*, TU Darmstadt, 2012.

47 P. Dugourd, R. Antoine, M. A. El Rahim, D. Rayane, M. Broyer and F. Calvo, *Chem. Phys. Lett.*, 2006, **423**, 13–16.

48 H. J. A. Jensen, R. Bast, T. Sau and L. Visscher, *DIRAC16*, 2016, `http://www.diracprogram.org/`.

49 K. G. Dyall, *Theor. Chem. Acc.*, 2002, **108**, 335–340.

50 K. G. Dyall, *Theor. Chem. Acc.*, 2006, **115**, 441–447.

51 K. G. Dyall, *Theor. Chem. Acc.*, 2004, **112**, 403–409.

52 N. Drebov, E. Oger, T. Rapps, R. Kelting, D. Schooss, P. Weis, M. M. Kappes and R. Ahlrichs, *J. Chem. Phys.*, 2010, **133**, 224302.

53 E. Oger, R. Kelting, P. Weis, A. Lechtken, D. Schooss, N. R. Crawford, R. Ahlrichs and M. M. Kappes, *J. Chem. Phys.*, 2009, **130**, 124305.

54 P. Schwerdtfeger, *ChemPhysChem*, 2011, **12**, 3143–3155.

55 T. A. Manz and N. G. Limas, *RSC Adv.*, 2016, **6**, 47771–47801.

56 T. A. Manz, *RSC Adv.*, 2017, **7**, 45552–45581.

57 W. Tang, E. Sanville and G. Henkelman, *J. Phys. Condens. Matter*, 2009, **21**, year.

58 Prof. Dr. Florian Müller-Plathe, *Biby Cluster Resources*, `http://www.chemie.tu-darmstadt.de/mueller-plathe/home/index.en.jsp`.